tent of 10 Å phase. In an earlier investigation (*2*), the composition was assumed to be $Mg_3Si_4O_{10}(OH)_2{\cdot}2H_2O$, but no direct compositional measurement was made. The Mg:Si ratio was later confirmed to be the same as in talc (*14*), but thermogravimetric analysis suggested a composition that was less rich in H_2O than previously suggested, $Mg_3Si_4O_{10}(OH)_2{\cdot}H_2O$. It was proposed that H_2O molecules occupied 12-fold coordinated interlayer sites between opposing tetrahedral layers in the talc structure and that the structure is stabilized through the interaction of each H_2O molecule with an octahedral-layer OH group to form H_3O^+ and O^{2-}. A subsequent study (*21*) argued against the necessity of neighboring OH groups to stabilize the interlayer H_2O and suggested that proton resonance between the interlayer O atoms and basal O atoms in the tetrahedral layers gives rise momentarily to OH^-, H_2O, H_3O^+, or a combination of these species. More recent weight-loss experiments (*7*) implied a composition that was even less rich in H_2O for 10 Å phase, $Mg_3Si_4O_{10}(OH)_2{\cdot}0.65H_2O$. Our thermogravimetric analysis has yielded the same H_2O content, $x = 0.65$ (*13*). These differences in previous values of measured H_2O content are accompanied by differences in measured position of the basal spacing diffraction peak, suggesting variable H_2O content depending on the pressure and temperature conditions of the synthesis or on the composition of the starting material. One feature that characterizes all previous studies is a broad basal spacing peak, in contrast to the sharpness of the talc peak. However, our in situ experiments, particularly 10Å-1, showed that, at high pressure and temperature, the 10 Å phase peak is identical in appearance to the talc peak (Fig. 3). It neither shows broadening, nor does it vary in position. Therefore, the variations seen in previous studies may be produced on quenching the sample, which might result in extra H_2O being incorporated in the interlayers, causing variable basal spacing. Our results therefore suggest that, within its stability field, 10 Å phase has a fixed structure. The difference in volume between talc and 10 Å phase is less than what would be expected if 10 Å phase contained two or three times as much H_2O as talc (*22*); instead, the difference is consistent with the composition $Mg_3Si_4O_{10}(OH)_2{\cdot}0.65H_2O$. The closeness of the extra $0.65H_2O$ to the value of two-thirds suggests a structural control on the interlayer H_2O content, filling two-thirds of the 12-fold coordinated interlayer sites.

Our results show that 10 Å phase could carry H_2O into the mantle in talc-bearing rocks in subduction zones beyond the depth at which talc breaks down. Our results are also important because the 10 Å phase problem is a tractable one whose conclusions may be applied to other, less accessible systems. We have shown that high-pressure and high-temperature hydration reactions can be observed in situ under dynamic conditions. This allows for the possibility of observing hydration reactions of other high-pressure mantle phases, perhaps revealing the stability of new phases, and also of observing reaction mechanisms and structural and volume relations between reactants and their hydrated products.

References and Notes

1. A. E. Ringwood and A. Major, *Earth Planet. Sci. Lett.* **2**, 130 (1967); L.-G. Liu, *Phys. Earth Planet. Inter.* **42**, 255 (1986); M. Kanzaki, *Phys. Earth Planet. Inter.* **66**, 307 (1991).
2. K. Yamamoto and S. Akimoto, *Am. J. Sci.* **277**, 288 (1977).
3. J. Gill, *Orogenic Andesites and Plate Tectonics* (Springer-Verlag, New York, 1981).
4. A. R. Pawley and B. J. Wood, *Am. Mineral.* **80**, 998 (1995). The upper pressure limit of 10 Å phase stability has not been determined, but it is at least 8 GPa (*2*).
5. M. Cannat, *J. Geophys. Res.* **98**, 4163 (1993).
6. C. E. Manning, *Int. Geol. Rev.* **37**, 1074 (1995).
7. B. Wunder and W. Schreyer, *J. Petrol.* **33**, 877 (1992).
8. S. M. Clark, *Nucl. Instrum. Methods Phys. Res.* **A381**, 161 (1996).
9. D. Walker, M. A. Carpenter, C. M. Hitch, *Am. Mineral.* **75**, 1020 (1990); D. Walker, *Am. Mineral.* **76**, 1092 (1991). We used tungsten carbide anvils with 12-mm truncated edge lengths.
10. T. Irifune *et al.*, *Science* **272**, 1468 (1996).
11. In a study by Ayers *et al.* [J. C. Ayers *et al.*, *Am. Mineral.* **77**, 1080 (1992)] and in ours, a watertight seal was formed when the sample was pressurized at low temperature during the experiment, and then the Pt alloyed with the Ti on heating. Leakage of some of the H_2O out of the capsule before pressurization resulted in a variable H_2O content during our experiments.
12. The Ti content of a sample run at 6.5 GPa and 700°C for 4 hours was determined by electron microprobe analysis. At a distance of 10 μm from the Ti wall, the Ti content was 0.25 weight %, and at a distance of 90 μm, it was <0.01 weight %.
13. N. J. Chinnery, thesis, University of Manchester, Manchester, UK (1999).
14. The volume behavior of talc at pressure and temperature conditions within the 10 Å phase stability field was measured in (*13*). The talc sample was mixed with NaCl, and diffraction patterns were collected at 4 to 6 GPa and 25° to 600°C. The pressure was determined with equation of state data for NaCl [D. L. Decker, *J. Appl. Phys.* **42**, 3239 (1971)]. Sodium chloride could not be mixed with the talc in this study because it would have dissolved in the H_2O in the capsule.
15. J. F. Bauer and C. B. Sclar, *Am. Mineral.* **66**, 576 (1981).
16. The convention that the repeat length of the unit cell along the *z* crystallographic axis in 10 Å phase is half that in talc results in (001) in 10 Å phase being equivalent to (002) in talc.
17. The relation between energy *E*, *d* spacing, and detector angle θ is given by the equation $d = 6.199/(E \sin \theta)$.
18. The composition of the talc, as analyzed by electron microprobe, is $Mg_{2.93}Fe_{0.03}Al_{0.01}Na_{0.01}Si_{4.00}$.
19. Experiments at 3 to 7 GPa and 200° to 700°C (*7*) suggested that 10 Å phase should break down to talc + H_2O at these conditions.
20. The position of the reaction talc + H_2O = 10 Å phase was found to extend from 730°C at 5.3 GPa to 580°C at 7 GPa [B. Wunder and W. Schreyer, *Lithos* **41**, 213 (1997)].
21. A. K. Miller, S. Guggenheim, A. F. Koster van Groos, *Am. Mineral.* **76**, 106 (1991).
22. Quench experiments on the 10 Å phase dehydration reaction, 10 Å phase = enstatite + coesite + H_2O, have shown it to have a negative value for dP/dT (the derivative of pressure with respect to temperature) (*13*). Applying the Clausius-Clapeyron equation, $dP/dT = \Delta S/\Delta V$, and assuming that the entropy change, ΔS, for this dehydration reaction is positive, we infer that the volume change, ΔV, is negative. Using estimated volumes of 10 Å phase from (*13*) and from A. R. Pawley, S. A. T. Redfern, B. J. Wood [*Contrib. Mineral. Petrol.* **122**, 301 (1995)] and volumes of enstatite, coesite, and H_2O from T. J. B. Holland and R. Powell [*J. Metamorph. Geol.* **16**, 309 (1998)], we calculated that ΔV can only be negative if less than $\sim 1.8H_2O$ per formula unit of 10 Å phase is released in the reaction.

23. This work was supported by Natural Environment Research Council (NERC) studentship GT4/95/223/E to N.J.C. and NERC grants GR3/10308 and GR3/11181 to A.R.P. We thank M. Henderson for helpful discussions and R. Jones for technical assistance.

22 July 1999; accepted 27 September 1999

Field-Effect Flow Control for Microfabricated Fluidic Networks

Richard B. M. Schasfoort, Stefan Schlautmann, Jan Hendrikse, Albert van den Berg*

The magnitude and direction of the electro-osmotic flow (EOF) inside a microfabricated fluid channel can be controlled by a perpendicular electric field of 1.5 megavolts per centimeter generated by a voltage of only 50 volts. A microdevice called a "flowFET," with functionality comparable to that of a field-effect transistor (FET) in microelectronics, has been realized. Two flowFETs integrated with a channel junction have been used to generate opposite flows inside a single EOF-pumped channel, thus illustrating the potential of the flowFET as a controlling and switching element in microfluidic networks.

Integrated microfluidic (μfluidic) devices are being used to automate the generation and analysis of chemical compounds (*1*–*6*). Chemical analyses on μfluidic devices can be highly automated and can reduce the consumption of reagents by several orders of magnitude (*7*–*9*). Miniaturized analysis systems depend on the precise control of fluids through the network. One approach is to use pressure-driven flows delivered by off-chip pressure

MESA+ Research Institute, University of Twente, Post Office Box 217, 7500 AE Enschede, Netherlands.

*To whom correspondence should be addressed.

sources or micropumps (*10*). However, in the great majority of μfluidic circuits, especially those that use electrophoretic separations, fluid flows are driven and directed using EOF (*11*). Electro-osmotic pumps offer a number of advantages over micromachined pressure-driven pumps, such as ease of fabrication and the absence of moving parts. Moreover, sample plugs suffer little from dispersion because the fluid velocity is nearly constant across the channel diameter. These pumps are usually controlled by manipulating the externally applied EOF-generating voltage. In this case, simultaneous control of EOF in channels connected with each other cannot easily be accomplished. The flow may also be controlled by manipulating the chemical composition of the buffer solution, thereby influencing the zeta potential (ζ), the potential difference across the mobile part of the electrical double layer of the channel wall. However, this method does not allow for a spatial- or time-controlled modification of ζ.

The principle of modifying and even reversing the EOF with a constant longitudinal field inside a capillary by a radial electrical field has already been presented (*12*). However, in those studies, fused silica capillaries were used and the purpose was the enhancement of the electrophoretic separation efficiency, rather than the control of flows in integrated devices. Moreover, the experiments were carried out in capillaries covered with a thin, ionically conductive polymer film, and the thickness of the capillary walls required high voltages (several kilovolts) to obtain sufficiently high radial electric fields.

Here, we present a method for controlling ζ of a micromachined channel by applying a small voltage over the channel wall. In EOF pumping, the surface of the channel (such as silica), when filled with a solution of pH > 3, becomes negatively charged as a result of the dissociation of its surface silanol groups. To provide overall charge neutrality, the fluid adjacent to the wall becomes positively charged so that an electrical double layer is formed and a potential difference across the interface is created (Fig. 1A). When a voltage is applied across the fluid at the two ends of the channel, the positive ions of the double layer move under the influence of the longitudinal electric field, E, with speed v_{EOF}, dragging the fluid with them through viscous coupling. This speed is related to E, ζ, and the permittivity ε and viscosity η of the fluid:

$$v_{EOF} = \frac{\varepsilon}{\eta}\zeta E \qquad (1)$$

We introduce a low-voltage flow control by means of modulation of v_{EOF} at constant longitudinal E by changing ζ of the channel wall (Fig. 1, B and C). A perpendicular electric field applied between a third electrical contact (at the outside of the channel wall) and the bulk of the fluid can create a local change of v_{EOF} independent of E. The controllable EOF that can be achieved by the longitudinal E can be combined with the ease of switching the ζ-controlled elements in the μfluidic circuitry. The function and operation of the device is roughly analogous to that of the solid-state field-effect transistor (FET) in integrated circuits, where an electric current is manipulated by a perpendicular field generated by a third electrode or gate electrode. In this setup, the ends of the channel play a role that is similar to the source and drain contacts of a FET. Therefore, the device presented here is called a "flowFET" and the electrode attached to the outside of the channel wall is called the gate electrode.

The three-capacitor model shown in Fig. 1D has been proposed (*12*) to estimate the magnitude of the effect. The gate voltage V_g can induce Δζ:

$$\Delta\zeta = \frac{C_{wall}}{C_d}V_g \qquad (2)$$

where C_{wall} is the capacitance of the channel wall and C_d is the capacitance of the electrical double layer. Because C_d increases with increasing |ζ| the relation between Δζ and V_g is more complicated than Eq. 2 suggests, and saturation occurs at high $|V_g|$ values (*13*). C_{wall} is inversely proportional to the wall thickness, implying that modulation of ζ with low voltages requires extremely thin walls (<1 μm).

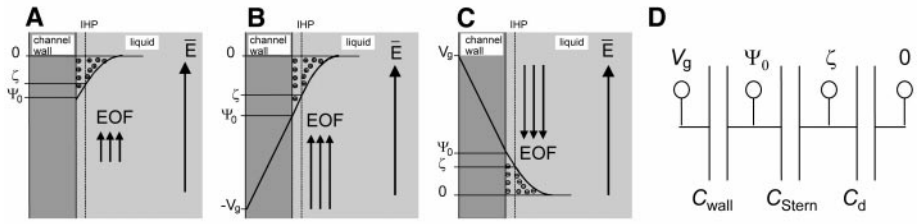

Fig. 1. (**A**) Illustration of the development of ζ and EOF at the interface between conductor (silicon), insulator (silicon nitride), and an electrolyte. (**B**) Influence of the application of an enhancing field over the channel wall. (**C**) Influence of an inverting field. Note that the field effect is proportional to the channel wall thickness as well as to V_g. (**D**) The three capacitors in series that are used to describe the effect of V_g on ζ. The Stern capacitance is neglected in the qualitative explanation given here. IHP, inner Helmholtz plane; Ψ_0, surface potential of the insulator surface.

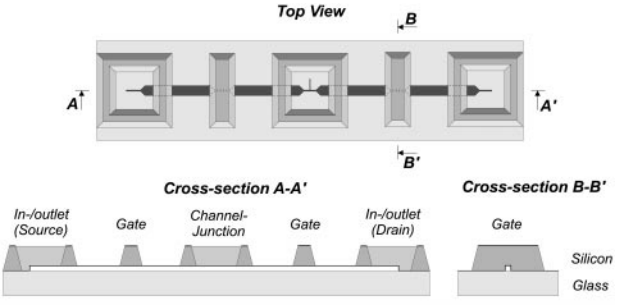

Fig. 2. Top view and cross section of the transparent insulated microchannel. The device is fabricated in three steps: (i) The channels are etched into a silicon wafer, which is then covered with a silicon nitride layer 390 nm thick. (ii) The silicon wafer is anodically bonded to a glass wafer. (iii) The semiconducting silicon is removed, leaving insulated silicon nitride microchannels. Note that the bottom of the gate area is not influenced by the gate electrode. Fluid reservoirs as well as gate contacts are defined by the patterned silicon that was not removed.

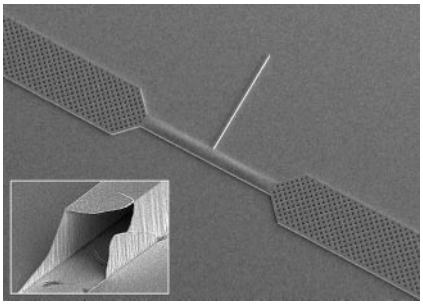

Fig. 3. SEM image of the channel junction region in the middle of the floating square reservoir. The low-resistance web-like supply channels (width 400 μm) are shown. The supply channels, 100 μm wide and 25 μm high, are visible, including the side channel (25 μm wide and 25 μm high). Inset: SEM picture of the side channel cross section, showing the insulating wall (390 nm thick).

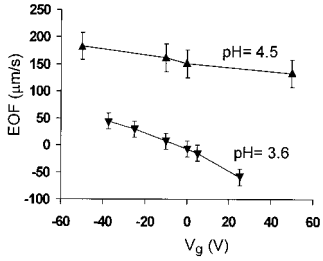

Fig. 4. EOF as a function of applied gate voltage V_g for a potential difference of 25 V (approximate longitudinal field strength of 30 V/cm) applied to channels filled with phosphate solutions having the indicated pH values. The addition of CTAB to the phosphate buffer modified ζ of the channel wall and shifted the point of zero EOF to higher pH values.

The currently used technique for fabrication of EOF devices, isotropic etching of channels into glass wafers (*7*), does not allow the creation of such very thin walls, and another approach is needed to manufacture these devices. Silicon microtechnology offers a broad scope of techniques, but the semiconducting character of silicon limits the use of higher voltages. Therefore, a technology for the fabrication of transparent insulated microchannels was developed at MESA$^+$, combining the design flexibility of silicon micromachining and the good insulation properties of glass (*14*). The fabrication steps (Fig. 2) yield microchannels surrounded by a thin, free-standing, and rather fragile silicon nitride sidewall. A scanning electron micrograph (SEM) image of the bare transparent insulated microchannels is shown in Fig. 3.

To demonstrate the possibility of EOF modulation in transparent insulated microchannels, we prepared straight single-flowFET structures that were filled via capillary action with 2 mM NaH_2PO_4/H_3PO_4 mixtures with pHs of 3.6 and 4.5. The red dye rhodamine B was added to the solution at one side of the channel so that fluid flow was displayed by the moving front between the two fluids. An EOF-generating voltage of 25 V (*15*) and gate voltages between −37.5 and 25 V were applied (*16*), and the flow velocity was determined by measuring the velocity of the red dye front in the channel between the inlet and the gate electrode using video imaging. The bottom of the channel remains unaffected and thereby reduces the overall measured effect. At a pH of 3.6, the EOF can be manipulated and its direction can even be reversed (Fig. 4). The fluid could be moved back and forth several times until the front became too diffuse to monitor properly. At higher pHs, the EOF could not be manipulated with equal ease, because of the larger intrinsically present double-layer charge at these pH values (as predicted by Eq. 2) and the remaining EOF at the supply channels, which leads to a less-effective manipulation of the net EOF. In addition, the EOF generated at the bottom of the microchannel that is not covered by the gate electrode diminishes the effect of the flowFET. Adding the EOF modifier *N*-cetyl-*N*,*N*,*N*-trimethyl ammonium bromide (CTAB, 0.01 mg/ml) to the buffer solution modifies ζ of the microchannel wall, so that the pH value is higher where the EOF is zero. In this situation, reversal of the EOF by a perpendicular electric field appeared possible at pH 7.4. The addition of CTAB broadens the scope for fluidic network applications by tuning the point of zero EOF in combination with flowFET control.

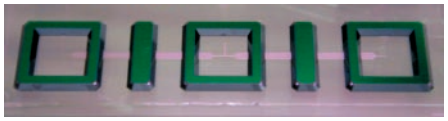

Fig. 5. Photograph showing two flowFETs integrated with a channel junction. Three square reservoirs for buffer solution containment and two gate contacts are shown (green areas). One electrode (source contact, grounded) was connected to the left reservoir and another electrode (drain contact, positive) to the right reservoir. The middle reservoir, which contains the channel junction, was kept floating and contains a drop of buffer solution. Both gate electrodes were connected to control the individual gate voltage. The silicon gate contact is connected to a gate electrode using a conducting glue. The web-like channel structures on the left and right sides of the T-junction in the middle (pink areas) serve as low-electric-resistance fluid reservoirs.

In a second experiment, the fluid flow was manipulated using two flowFETs (Fig. 5) connected to each other at a channel T-junction (Fig. 3). The two flowFETs at the left and right sides were used to direct the flow across the junction. The channels were filled with the red and transparent pH 3.6 solutions, as described above, and a voltage of 50 V was applied between the right and left ends of the channel to generate a slow EOF that went from right to left. The short side channel was left electrically floating, and the complete junction was covered by a droplet of transparent buffer solution to prevent the aspiration of bubbles into the channel and to show the flow of the red dye out of the open side channel. Initially, the EOF was enhanced by applying −50 V between both the left and gate contacts and the respective ends of the channel to enhance the EOF, and the dye was allowed to pass the junction. After 11 s, +50 V was applied between the left gate contact and the left end of the channel, but without changing the magnitude and direction of the field in the longitudinal channel; hence, the flow in this part of the channel was reversed and two opposite EOFs were created within one single channel. In this way, the dye at the junction was pushed out through the side channel and into the surrounding liquid. A time sequence of the dispensing of a plug into the side channel is shown in Fig. 6, A to C.

These results show that it is possible to manipulate fluids driven by electro-osmotic flow through μfluidic networks by manipulation of ζ at the channel wall of a flowFET. No adverse effects, such as heating or electrolysis, were observed. This approach enables the fast manipulation of fluids where a constant driving longitudinal electrokinetic voltage is applied at a limited number of inlets (*17*).

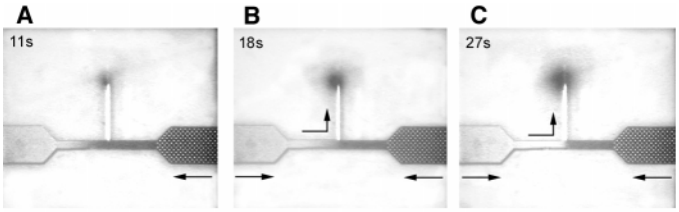

Fig. 6. Sequence of video frames showing the pushing of red rhodamine B dye into an open side channel. (**A**) When both flowFETs are in enhancement mode ($V_g = -50$ V), the fluid moves toward the left. (**B**) The left flowFET is switched to the inversion mode ($V_g = +50$ V) so that the fluid in the left channel moves toward the right while the fluid in the right channel still moves toward the left. Red dye is being pushed through the side channel. (**C**) More red dye has been pushed out of the side channel, and a sharp front between the dyed and blank solutions has been created. Note that the vertical side channel looks white as a result of optical reflection.

References and Notes

1. R. F. Service, *Science* **282**, 396 (1998); M. Freemantle, *Chem. Eng. News* **77**, 27 (22 February 1999).
2. W. Ehrfeld, Ed., *Proceedings of the First International Conference on Microreaction Technology*, Frankfurt, Germany, 23–25 February (Springer, Berlin, 1997).
3. W. H. Moos, in *A Practical Guide to Combinatorial Chemistry*, A. W. Czarnik and S. H. DeWitt, Eds. (American Chemical Society, Washington, DC, 1997), pp. 1–16.
4. D. J. Harrison and A. van den Berg, Eds., *Micro Total Analysis Systems* (Kluwer Academic, Dordrecht, Netherlands, 1998).
5. C. H. Mastrangelo, M. A. Burns, D. T. Burke, *Proc. IEEE* **86**, 1769 (1998).
6. E. Jacobs, E. Vadasdi, L.-N. Coman, *Clin. Chem.* **39**, 1069 (1993).
7. D. J. Harrison *et al.*, *Science* **261**, 895 (1993).
8. A. van den Berg and T. S. J. Lammerink, *Top. Curr. Chem.* **194**, 21 (1998); B. H. Weigl and P. Yager, *Science* **283**, 346 (1999); M. U. Kopp, A. J. de Mello, A. Manz, *Science* **280**, 1046 (1998); B. He, N. Tait, F. Regnier, *Anal. Chem.* **70**, 3790 (1998).
9. M. A. Burns *et al.*, *Science* **282**, 484 (1998); L. C. Waters *et al.*, *Anal. Chem.* **70**, 158 (1998).
10. S. C. Jacobson, R. Hergenröder, L. B. Koutny, R. J. Warmack, J. M. Ramsey, *Anal. Chem.* **66**, 1107 (1994); A. T. Woolley and R. A. Mathies, *Proc. Natl. Acad. Sci. U.S.A.* **91**, 11348 (1994); C. S. Effenhauser, A. Manz, H. M. Widmer, *Anal. Chem.* **67**, 2284 (1995); S. C. Jacobson and J. M. Ramsey, in *Handbook of Capillary Electrophoresis,* J. P. Landers, Ed. (CRC Press, Boca Raton, FL, 1997), pp. 827–840.
11. H. Gau, S. Herminghaus, P. Lenz, R. Lipowsky, *Science* **283**, 46 (1999); B. S. Gallardo *et al.*, *Science* **283**, 57 (1999).
12. C. S. Lee, W. C. Blanchard, C.-T. Wu, *Anal. Chem.* **62**, 1550 (1990); M. A. Hayes and A. G. Ewing, *Anal. Chem.* **64**, 512 (1992); K. Ghowsi and R. J. Gale, *J. Chromatogr.* **559**, 95 (1991); C. T. Wu, T. Lopes, B.-C. S. Lee, *Anal. Chem.* **64**, 886 (1992); M. A. Hayes, I. Khetarpal, A. G. Ewing, *Anal. Chem.* **65**, 2010 (1993); *Anal. Chem.* **65**, 27 (1993).
13. Because the capacitance of a channel with inner area *A* is given by
$$C_d = 228.5 \times 10^{-6} A\sqrt{c}\cosh(19.46\zeta)$$
where *c* is the concentration of electrolyte ions, Eq. 2 predicts that it is more difficult to modulate ζ of solutions having a high electrolyte concentration. The fast rise of C_d with ζ limits the possibilities of manipulation to moderate ζ only, an effect that was not taken into account when the three-capacitor model was first presented.
14. R. W. Tjerkstra *et al.*, *Proceedings of The Tenth Annual International Workshop on Micro Electro Mechanical Systems* (IEEE, Piscataway, NJ, 1997), p. 147; Y. Fintschenko, P. Fowler, V. Spiering, G.-J. Burger, A. van den Berg, in *Micro Total Analysis Systems*, D. J. Harrison and A. van den Berg, Eds. (Kluwer Academic, Dordrecht, Netherlands, 1998), pp. 327–330; Y. Fintschenko and A. van den Berg, *J. Chromatogr. A* **819**, 3 (1998).

15. In separate experiments, EOF-generating fields of up to 700 V/cm have been applied to transparent insulated microchannels without flowFETs. Gate voltages of 100 V (equal to fields as large as 2.6 MV/cm) have been applied to channel walls before electrical breakthrough occurred.
16. In accordance with the tradition of reporting gate voltages in metal-oxide semiconductor FETs, the potential difference between the gate contact and the end of the channel is reported. The actual potential difference between the gate contacts and the fluid opposite them differs from the reported voltages by an amount equal to the potential drop in the channel between the flowFET gate and the end of the channel. This depends on the exact channel geometry and is estimated to be around 12.5 V.
17. A. van den Berg, Netherlands Patent NL-1010327, priority date 15 October 1998.

2 June 1999; accepted 24 September 1999

Organic-Inorganic Hybrid Materials as Semiconducting Channels in Thin-Film Field-Effect Transistors

C. R. Kagan, D. B. Mitzi, C. D. Dimitrakopoulos

Organic-inorganic hybrid materials promise both the superior carrier mobility of inorganic semiconductors and the processability of organic materials. A thin-film field-effect transistor having an organic-inorganic hybrid material as the semiconducting channel was demonstrated. Hybrids based on the perovskite structure crystallize from solution to form oriented molecular-scale composites of alternating organic and inorganic sheets. Spin-coated thin films of the semiconducting perovskite $(C_6H_5C_2H_4NH_3)_2SnI_4$ form the conducting channel, with field-effect mobilities of 0.6 square centimeters per volt-second and current modulation greater than 10^4. Molecular engineering of the organic and inorganic components of the hybrids is expected to further improve device performance for low-cost thin-film transistors.

Alternative semiconducting materials for thin-film field-effect transistors (TFTs), which have mobilities at least comparable to that of amorphous silicon (a-Si) and may also be easily processed with low-cost techniques, are required to enable new opportunities for display and storage technologies. Conjugated organic small molecules (*1–4*), short-chain oligomers (*5, 6*), and long-chain polymers (*7–10*) continue to receive substantial attention as new semiconducting channels for TFTs. Organic semiconductors may be deposited by low-cost, low-temperature processes such as spin coating, dip coating, or screen printing from solution or thermal evaporation. These techniques provide a potential niche for organic semiconductors in applications that require large areas, low cost, mechanical flexibility, or a combination of these factors. Examples of applications include TFTs for active matrix liquid crystal displays (AMLCDs), where a-Si is presently used; active matrix organic light-emitting diodes (AMOLEDs); and low-cost data storage devices. In addition, low-temperature deposition conditions enable organic semiconductors to be deposited on plastic substrates for flexible electronic devices (*11, 12*).

In organic semiconductors, π-orbital overlap between adjacent conjugated molecules enables charge transport, but the weak van der Waals interaction bonding neighboring molecules limits their carrier mobilities. The highest mobilities reported for organic TFTs have been achieved by vacuum evaporation of ordered thin films of either small molecules (*3*) or short-chain oligomers (*6*). Molecular ordering improves orbital overlap and therefore film mobility. Although evaporated films demonstrate mobilities comparable to that of a-Si (0.1 to 1 $cm^2/V \cdot s$), the high vacuum used makes deposition costly. Solution-based deposition techniques, such as spin coating, are the most desirable processes because they are both cheap and large-area deposition methods. Long-chain polymers are soluble enough to be spin coated, but their mobilities, 10^{-8} to 10^{-2} $cm^2/V \cdot s$, are lower because films are more disordered (*9*). Recently a soluble pentacene precursor was synthesized and converted to yield mobilities of 0.1 $cm^2/V \cdot s$ (*4*). The low carrier mobilities of organic TFTs limit their device-switching speeds and therefore their range of potential applications.

Organic-inorganic hybrid materials combine the advantageous properties characteristic of crystalline inorganic solids with those of organic molecules within a molecular-scale composite. The inorganic component forms an extended framework bound by strong covalent or ionic (or both) interactions to provide high carrier mobilities. The organic component facilitates the self-assembly of these materials, enabling hybrids to be deposited by the same simple, low-cost, low-temperature processes as the organic materials. The organic component is also used to tailor the electronic properties of the inorganic framework by defining its reduced dimensionality and by mediating the electronic coupling between inorganic units. Engineering the organic-inorganic hybrid on the molecular scale may be done to maximize both field-effect mobility and current modulation. The combination of high carrier mobility and ease of processing may make organic-inorganic hybrid materials good substitutes in all the applications put forth for organic materials. The potentially higher carrier mobilities of hybrid materials may extend their application to higher speed devices than is presently possible with either a-Si or organic semiconductors.

One class of organic-inorganic hybrid is based on the three-dimensional (3D) perovskite structure ABX_3 (Fig. 1). The chemistry of the organic and inorganic components of the perovskite can be tailored to tune the electronic, optical, magnetic, and mechanical properties of hybrid materials (*13*). Although most organic-inorganic perovskites are insulating, hybrids having a tin(II) iodide framework are electrically conductive. Hall measurements on pressed pellet samples of the 3D perovskite $CH_3NH_3SnI_3$ reveal that it is a low-carrier-density metal with a room temperature Hall mobility of 50 $cm^2/V \cdot s$ (*14*). Layered perovskites of the form $A_2A'_{n-1}Sn_nI_{3n+1}$ may also be prepared by stacking n inorganic layers, containing a small A′ cation, separated by organic layers of a larger A cation. Systematic study of the effects of dimensionality has shown a metal-to-semiconductor transition as n is reduced from $n \rightarrow \infty$ for the 3D hybrid to $n = 1$, for the 2D layered hybrid (*15*). Although the conductivity is reduced with decreasing dimensionality, high carrier mobilities are expected for the layered perovskites because they consist of the same extended inorganic framework of corner-sharing SnI_6 octahedra that gives rise to the high carrier mobility of the 3D analog $CH_3NH_3SnI_3$.

We demonstrated an organic-inorganic TFT using the 2D layered organic-inorganic perovskite $(C_6H_5C_2H_4NH_3)_2SnI_4$ as the semiconducting channel. $(C_6H_5C_2H_4NH_3)_2SnI_4$ is synthesized by dissolving stoichiometric quantities of SnI_2 and the organic salt, $C_6H_5C_2H_4NH_2 \cdot HI$ in concentrated (57 weight %) aqueous HI at 90°C under flowing N_2. Crystals of the compound $(C_6H_5C_2H_4NH_3)_2SnI_4$ precipitate from solution upon cooling to room temperature. The crystals are filtered, rinsed in 5:1 toluene:*n*-butanol, and dried under vacuum. The crystals are redissolved at 20 mg/ml in anhydrous methanol. Solutions are filtered through a 0.2-μm polytetrafluoroethylene filter and spun onto wafers at 2500 rpm for 2 min in an inert atmo-

IBM T. J. Watson Research Center, Post Office Box 218, Yorktown Heights, NY, 10598, USA.